nature immunology

Article

https://doi.org/10.1038/s41590-023-01720-w

The transcriptional cofactor Tle3 reciprocally controls effector and central memory CD8$^+$ T cell fates

Received: 17 January 2023

Accepted: 28 November 2023

Published online: 18 January 2024

Check for updates

Xin Zhao[1,7], Wei Hu[1,7], Sung Rye Park[1,7], Shaoqi Zhu[2,7], Shengen Shawn Hu[3], Chongzhi Zang[3,4], Weiqun Peng[2], Qiang Shan[5] ✉ & Hai-Hui Xue[1,6] ✉

Antigen-experienced CD8$^+$ T cells form effector and central memory T cells (T_{EM} and T_{CM} cells, respectively); however, the mechanism(s) controlling their lineage plasticity remains incompletely understood. Here we show that the transcription cofactor Tle3 critically regulates T_{EM} and T_{CM} cell fates and lineage stability through dynamic redistribution in antigen-responding CD8$^+$ T cell genome. Genetic ablation of *Tle3* promoted CD8$^+$ T_{CM} cell formation at the expense of CD8$^+$ T_{EM} cells. Lineage tracing showed that Tle3-deficient CD8$^+$ T_{EM} cells underwent accelerated conversion into CD8$^+$ T_{CM} cells while retaining robust recall capacity. Tle3 acted as a coactivator for Tbet to increase chromatin opening at CD8$^+$ T_{EM} cell-characteristic sites and to activate CD8$^+$ T_{EM} cell signature gene transcription, while engaging Runx3 and Tcf1 to limit CD8$^+$ T_{CM} cell-characteristic molecular features. Thus, Tle3 integrated functions of multiple transcription factors to guard lineage fidelity of CD8$^+$ T_{EM} cells, and manipulation of Tle3 activity could favor CD8$^+$ T_{CM} cell production.

CD8$^+$ T lymphocytes have essential roles in mounting protective cellular immune responses against pathogens and malignantly transformed cells. A productive CD8$^+$ T cell response clears pathogens and forms memory CD8$^+$ T cells, which have heightened protective capacity than naive CD8$^+$ T cells[1]. Memory CD8$^+$ T cells consist of heterogeneous subsets, with distinct distribution patterns and functionality[2,3]. Compared with CD62L$^-$CD8$^+$ T_{EM} cells, which are largely detected in circulation, CD62L$^+$CD8$^+$ T_{CM} cells are more enriched in the secondary lymphoid organs, persist for a longer time and respond more robustly to rechallenge by the same pathogen[3,4]. In terms of their developmental origin, CD8$^+$ T_{CM} cells are derived from multiple sources, including CD8$^+$ T_{EM} cells[5] and various effector CD8$^+$ T cell subsets with elevated expression of interleukin (IL)-7Rα, CD62L and/or Tcf1 (refs. 6–10). However, the molecular mechanisms underlying lineage plasticity of memory CD8$^+$ T cells remain unknown.

Transcription factors orchestrate the differentiation of effector and memory CD8$^+$ T cells[11,12]. One mechanism is through their dynamic expression: Tbet and Blimp1 are induced in CD8$^+$ effector T (T_{eff}) cells and partly retained in memory CD8$^+$ T cells, while Tcf1 and Myb are downregulated in CD8$^+$ T_{eff} cells but partly restored in memory CD8$^+$ T cells[7,13–15]. Another mechanism is to utilize cofactors to achieve regulatory specificity, stability and transcriptional output, which is particularly important for stably expressed transcription factors such as Runx3 (refs. 16,17). The transcription cofactor Tle interacts with many transcription factors involved in the regulation of immune processes, including Tcf1/Lef1, Runx1/Runx3, Myc and Blimp1 (refs. 18–21).

[1]Center for Discovery and Innovation, Hackensack University Medical Center, Nutley, NJ, USA. [2]Department of Physics, The George Washington University, Washington, DC, USA. [3]Center for Public Health Genomics, University of Virginia School of Medicine, Charlottesville, VA, USA. [4]Department of Public Health Sciences, University of Virginia, Charlottesville, VA, USA. [5]National Key Laboratory of Immunity and Inflammation, Suzhou Institute of Systems Medicine, Chinese Academy of Medical Sciences & Peking Union Medical College, Suzhou, China. [6]New Jersey Veterans Affairs Health Care System, East Orange, NJ, USA. [7]These authors contributed equally: Xin Zhao, Wei Hu, Sung Rye Park, Shaoqi Zhu. ✉e-mail: shanq2009@gmail.com; haihui.xue@hmh-cdi.org

Tle proteins are the mammalian homologs of the *Drosophila* transcriptional repressor Groucho. There are four mammalian Tle genes, *Tle1*–*Tle4*, which encode full-length Tle proteins with unique and redundant functions in organogenesis including hematopoiesis[22–25]. *Tle3* is most abundantly expressed in T cells, followed by *Tle4* and *Tle1*, with *Tle2* at a barely detectable level[26]. *Tle1*, *Tle3* and *Tle4* critically regulate CD8$^+$ T cell lineage choice during thymic development in a gene dose-dependent manner[26]. In this study, we found that Tle3 was dynamically redistributed in the T cell genome during effector and memory CD8$^+$ T cell differentiation and that Tle3 functioned as an integrator of multiple transcription factors to reciprocally control CD8$^+$ T_{EM} and CD8$^+$ T_{CM} cell fates and lineage plasticity.

Results

Loss of Tle3 enhances CD8$^+$ T_{CM} cell formation

Because of the known functional redundancy among Tle proteins[25,26], we crossed the *Gzmb-Cre* transgene to mice carrying floxed alleles for *Tle1*, *Tle3* and *Tle4* (refs. 26–28) to ablate these genes in activated mature CD8$^+$ T cells without perturbing thymopoiesis. We obtained *Gzmb-Cre*$^+$*Rosa26*^{GFP}*Tle1*$^{fl/fl}$*Tle3*$^{fl/fl}$*Tle4*$^{fl/fl}$ mice and *Gzmb-Cre*$^-$*Rosa26*^{GFP}*Tle1*$^{fl/fl}$*Tle3*$^{fl/fl}$*Tle4*$^{fl/fl}$ littermate controls (hereafter *Tle134*$^{-/-}$ and wild-type (WT) mice, respectively), with *Rosa26*^{GFP} marking *Tle* gene-deleted cells. WT and *Tle134*$^{-/-}$ mice were infected with lymphocytic choriomeningitis virus (LCMV) Armstrong strain (LCMV-Arm) to elicit acute viral infection. On day 8 after infection, *Tle134*$^{-/-}$ mice showed >80% reduction in the frequency and numbers of CD8$^+$ T_{eff} cells, detected as antigen-experienced polyclonal CD11a^{hi}CD8^{lo} CD8$^+$ T cells or LCMV GP33 epitope-specific CD8$^+$ T cells, measured with GP33-tetramers or interferon (IFN)-γ-producing cells by GP33 peptide stimulation, compared to WT mice (Fig. 1a), demonstrating more profound impact on CD8$^+$ T_{eff} cells than ablation of Runx3, Tbet or Blimp1 alone[7,13,17,29].

We next investigated whether a specific Tle protein could fine-tune specific CD8$^+$ T cell functions that could not be compensated by its coexpressed homologs. We focused on Tle3 because of its abundant expression in naive CD8$^+$ naive T (T_N) cells and CD8$^+$ T_{eff} cells (Fig. 1b) and generated P14$^+$*Gzmb-Cre*$^+$*Rosa26*^{GFP}Tle3$^{fl/fl}$ (hereafter *Tle3*$^{-/-}$) and P14$^+$*Gzmb-Cre*$^+$*Rosa26*^{GFP}*Tle3*$^{+/+}$ (hereafter WT) mice, in which the transgenic P14 T cell antigen receptor (TCR) is specific for the LCMV GP33 epitope. WT or *Tle3*$^{-/-}$ CD45.2$^+$P14$^+$ T_N cells were adoptively transferred into CD45.1 WT mice, which were infected with LCMV-Arm the next day (Extended Data Fig. 1a). On day 8 after infection, *Tle3*$^{-/-}$ CD8$^+$ T_{eff} cells showed ~3-fold reduction in numbers (Fig. 1c), a modest 10% decrease in IFN-γ production and similar tumor necrosis factor (TNF) or granzyme B expression compared to WT CD8$^+$ T_{eff} cells (Extended Data Fig. 1b–d). The frequencies of fully differentiated KLRG1^{hi}IL-7Rα$^-$CD8$^+$ T_{eff} cells and KLRG1^{lo}IL-7Rα$^+$CD8$^+$ memory precursor T (T_{MP}) cells were similar between WT and *Tle3*$^{-/-}$ P14$^+$CD8$^+$ T cells (Fig. 1d). At the contraction phase (day 14 after infection), annexin V$^+$ apoptotic cells were reduced by ~50% in *Tle3*$^{-/-}$ CD8$^+$ T cells compared to WT CD8$^+$ T cells (Fig. 1c). At day 30 after infection, WT and *Tle3*$^{-/-}$ memory CD8$^+$ T cells were detected at similar numbers (Fig. 1c), but the frequency and numbers of *Tle3*$^{-/-}$ CD62L$^+$CD8$^+$ T_{CM} cells almost doubled compared to those of WT CD62L$^+$CD8$^+$ T_{CM} cells (Fig. 1f). *Tle3*$^{-/-}$ CD8$^+$ T_{CM} and T_{EM} cells showed similar capacity of producing multiple cytokines, including IFN-γ, TNF and IL-2, and had a 10–20% reduction in granzyme B expression compared with their WT counterparts (Fig. 1g,h). To investigate whether the phenotypic changes in *Tle3*$^{-/-}$ memory CD8$^+$ T cells were due to persistence of viral antigens, we collected sera and detected similar levels of LCMV by quantitative PCR with reverse transcription (RT–qPCR) or plaque assays in recipients of *Tle3*$^{-/-}$ or WT P14$^+$CD8$^+$ T cells on day 4 after infection, while viral titers on days 8, 14 and 30 after infection were below the detection limit (Extended Data Fig. 1e–g). Additionally, we performed co-transfer of *Tle3*$^{-/-}$ CD45.2$^+$ and WT CD45.1$^+$CD45.2$^+$P14$^+$CD8$^+$ T cells into CD45.1 WT mice, which were infected with LCMV-Arm the next day. On day 30 after infection, the frequency of *Tle3*$^{-/-}$ CD8$^+$ T_{CM} cells was ~3-fold higher than that of WT CD8$^+$ T_{CM} cells (Extended Data Fig. 1h), suggesting that propensity of *Tle3*$^{-/-}$ memory CD8$^+$ T cells toward T_{CM} cell formation was cell intrinsic. These functional analyses indicated that deletion of *Tle3* promoted the formation of CD8$^+$ T_{CM} cells.

We then performed single-cell RNA sequencing (scRNA-seq) on WT and *Tle3*$^{-/-}$ memory CD45.2$^+$CD8$^+$ T cells sorted from the CD45.1 recipient mice on day 30 after infection. Focused analysis of WT memory CD8$^+$ T cells identified three major populations and a minor population of few cells that were *Dock2*^{hi}, previously associated with 'virtual memory' T cells[30] (Fig. 2a,b). One major population was highly enriched in CD8$^+$ T_{CM} cell-characteristic genes, including *Sell* (encoding CD62L), *Ccr7*, *Il7r* and *Tcf7* (encoding Tcf1; Fig. 2c), which we defined as T_{CM} cells (Fig. 2a). The other two major populations had high expression of CD8$^+$ T_{EM} cell-characteristic genes, including *Klrg1*, *Cx3cr1*, *Zeb2* and *Bhlhe40*, which we defined as $T_{EM}1$ and $T_{EM}2$ cells, with the latter being *Klre1*^{hi} (Fig. 2b,c). Pseudotime trajectory analysis with Monocle[31] suggested maturation of $T_{EM}2$ to $T_{EM}1$ and then to T_{CM} cells (Fig. 2d), consistent with previous reports[5]. When combined, WT and *Tle3*$^{-/-}$ memory CD8$^+$ T cells were resolved into seven clusters, with cluster 7 as *Dock2*^{hi} (Fig. 2e). WT and *Tle3*$^{-/-}$ memory CD8$^+$ T cells were distributed in almost exclusive clusters among the other six major clusters (Fig. 2f), suggesting transcriptomic divergence due to Tle3 deficiency. Clusters 1–3 were mostly WT cells (Fig. 2g), with cluster 3 equivalent to T_{CM} cells, expressing T_{CM} cell-characteristic genes including *Tcf7*, *Sell*, *Ccr7*, *Il7r* and *Myc* (Fig. 2h). Clusters 4–6 were predominantly *Tle3*$^{-/-}$ cells, with cluster 4 expressing T_{EM} cell-characteristic genes including *Cx3cr1*, *Klrg1*, *Gzma*, *S1pr5* and *Bhlhe40*, while clusters 5 and 6 resembled cluster 3 (Fig. 2g,h). By assessing the collective behavior of single-cell-based CD8$^+$ T_{CM} and CD8$^+$ T_{EM} cell signature genes (Supplementary Table 1), the WT-predominant cluster 3 and *Tle3*$^{-/-}$-predominant clusters 5 and 6 were enriched in T_{CM} scores, but depleted of T_{EM} scores (Extended Data Fig. 2). These analyses indicated that loss of Tle3 facilitated acquisition of CD8$^+$ T_{CM} cell transcriptomic features at the single-cell level.

Tle3 promotes T_{EM} and suppresses T_{CM} signature genes

We next used multiomics approaches to investigate how Tle3 regulated CD8$^+$ T_{CM} and T_{EM} cell-characteristic molecular features. Because *Tle3*$^{-/-}$ memory CD8$^+$ T cells showed altered expression of T_{EM} cell-associated marker proteins such as KLRG1 and CX3CR1 (Extended Data Fig. 3a), we used the CD62L-based classical definition to sort CD62L$^-$CD8$^+$ T_{EM} and CD62L$^+$CD8$^+$ T_{CM} cells from the immune mice on day 30 after infection with LCMV-Arm (Extended Data Fig. 3b). We first performed bulk RNA-seq analysis to increase transcript sequencing depth. Principal component analysis (PCA) placed WT CD8$^+$ T_{EM} cells, *Tle3*$^{-/-}$ CD8$^+$ T_{EM} cells, WT CD8$^+$ T_{CM} cells and *Tle3*$^{-/-}$ CD8$^+$ T_{CM} cells in distinct clusters (Fig. 3a). Comparison between WT CD8$^+$ T_{CM} and WT CD8$^+$ T_{EM} cells identified 181 T_{CM} cell signature genes, including *Id3*, *Eomes*, *Irf8* and *Vcam1* (not captured by scRNA-seq), in addition to *Sell*, *Ccr7*, *Il7r* and *Tcf7*, and 90 T_{EM} cell signature genes, such as *Cx3cr1* and *Klrg1* (Fig. 3b and Supplementary Table 2). Together with differentially expressed genes (DEGs) comparing WT and *Tle3*$^{-/-}$ CD8$^+$ T_{CM} cells and those comparing WT and *Tle3*$^{-/-}$ CD8$^+$ T_{EM} cells (Extended Data Fig. 3c,d), a total of 1,272 DEGs were resolved into five expression clusters (ExpC1–ExpC5; Fig. 3c and Supplementary Table 3) by unsupervised *k*-means clustering analysis. Consistent with the known corepressor function of Tle3, ExpC1 and ExpC2 genes showed increased expression in *Tle3*$^{-/-}$ CD8$^+$ T_{CM} and *Tle3*$^{-/-}$ CD8$^+$ T_{EM} cells (defined as 'Tle3-repressed genes'), with T_{CM} cell signature genes more enriched in ExpC2 (Fig. 3c). Loss of Tle3 caused downregulation of many genes distributed in ExpC3–ExpC5 (defined as 'Tle3-actived genes'), with T_{EM} cell signature genes more enriched in ExpC5 (Fig. 3c). Gene-set enrichment analysis (GSEA) indicated that *Tle3*$^{-/-}$ CD8$^+$ T_{EM} cells were depleted of T_{EM} cell signature genes but were strongly enriched in T_{CM} cell signature genes (Fig. 3d,e). At the protein

https://doi.org/10.1038/s41590-023-01720-w

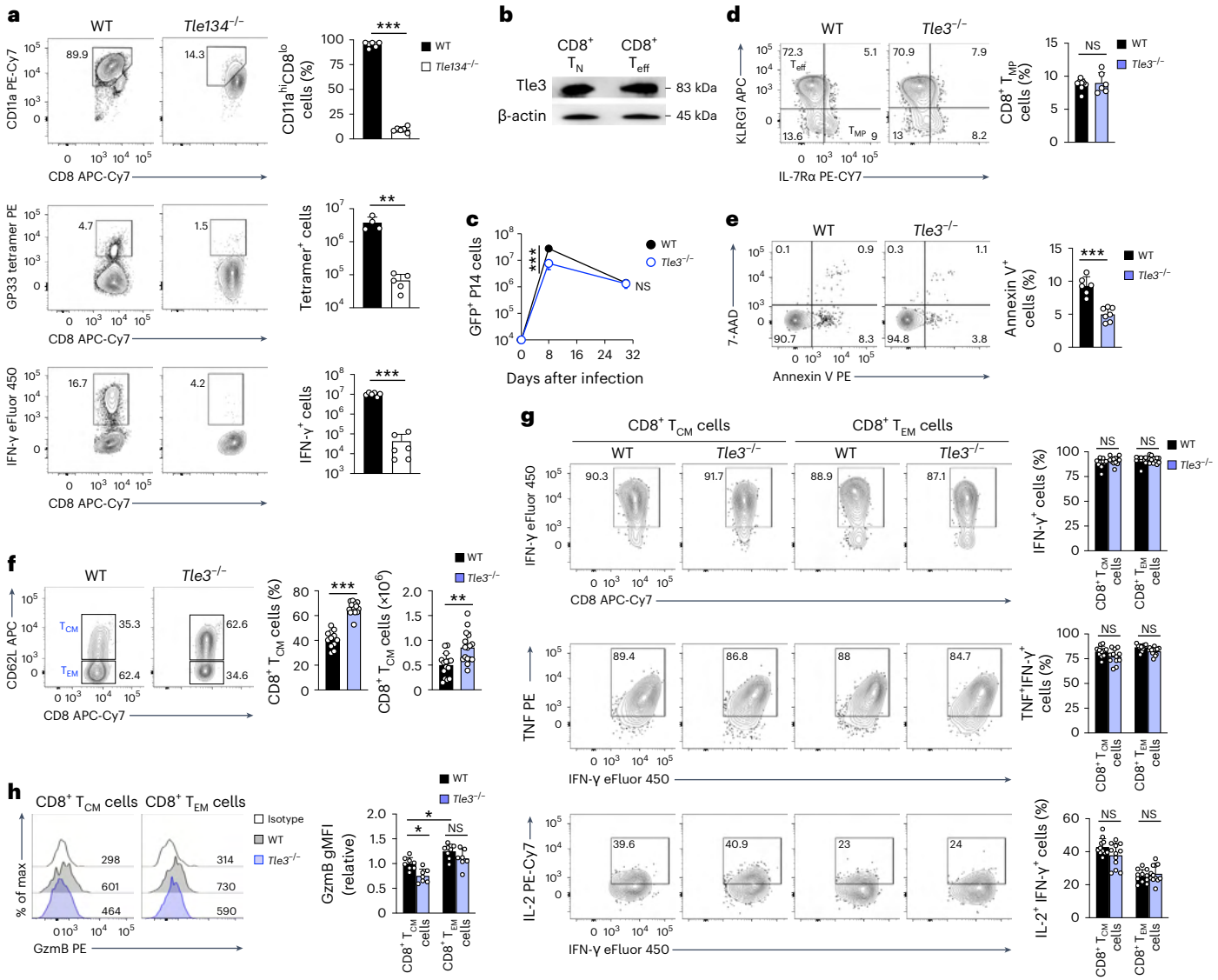

Fig. 1 | Targeting Tle3 favors generation of T_{CM} cells in response to acute viral infection. a, Representative flow cytometry plots of antigen-specific $CD8^+$ T cells in WT and *Tle134*$^{-/-}$ mice on day 8 after infection with LCMV-Arm, using CD11a surrogate marker, GP33-tetramer and GP33 peptide-stimulated IFN-γ production, and bar graphs showing cumulative data of frequency of antigen-experienced $CD8^+$ T cells or numbers of GP33-specific $CD8^+$ T cells. **b**, Immunoblot of Tle3 in $CD8^+$ T_N cells from uninfected WT mice and $CD8^+$ T_{eff} cells sorted on day 8 after infection with LCMV-Arm. Data are representative of two independent experiments. **c**, Numbers of WT or *Tle3*$^{-/-}$ $CD45.2^+P14^+CD8^+$ T cells identified on days 8 and 30 after infection in the spleens of CD45.1 WT recipient mice that were adoptively transferred with WT or *Tle3*$^{-/-}$ $CD45.2^+P14^+CD8^+$ T_N cells and infected with LCMV-Arm the next day. WT ($n = 7$) and *Tle3*$^{-/-}$ ($n = 7$) from three independent experiments. **d**, Representative flow cytometry plots of WT and *Tle3*$^{-/-}$ $KLRG1^{hi}IL\text{-}7R\alpha^-CD8^+$ T_{eff} cells and $KLRG1^{lo}IL\text{-}7R\alpha^+CD8^+$ T_{MP} cells on day 8 after infection in mice as in **c**, and bar graph showing cumulative data of $CD8^+$ T_{MP} cell frequency. **e**, Representative flow cytometry plots of cell viability of $P14^+CD8^+$ T cells on day 14 after infection in mice as in **c**, and bar graphs showing cumulative data of frequency of annexin V^+ cells. **f**, Representative flow cytometry plots of WT and *Tle3*$^{-/-}$ $CD62L^+CD8^+$ T_{CM} and $CD62L^-CD8^+$ T_{EM} cells at ≥ day 30 after infection in mice as in **c**, and bar graphs showing cumulative data of $CD8^+$ T_{CM} cell frequency and numbers. **g**, Representative flow cytometry plots of GP33-induced production of IFN-γ, TNF and IL-2 in $CD8^+$ T_{CM} and $CD8^+$ T_{EM} cells at ≥ day 30 after infection in mice as in **c**, and bar graphs showing cumulative data of the frequency of IFN-γ-producing cells in $CD8^+$ T_{CM} and $CD8^+$ T_{EM} cells, and that of TNF- and IL-2-producing cells in $IFN\text{-}\gamma^+$ $CD8^+$ T_{CM} and $CD8^+$ T_{EM} cells. **h**, Expression of granzyme B in $CD8^+$ T_{CM} and $CD8^+$ T_{EM} cells at ≥ day 30 after infection in mice as in **c**, and bar graphs showing cumulative data of relative geometric mean fluorescence intensity (gMFI) of granzyme B, where the granzyme B gMFI in WT $CD8^+$ T_{CM} cells was set as 1 in each experiment, and that in other cell types was normalized accordingly. Data in **a** and **d**–**h** are representative of 2–3 independent experiments, and all cumulative data in **a** and **c**–**h** are means ± s.d., with individual data points shown. $^*P < 0.05$; $^{**}P < 0.01$; $^{***}P < 0.001$; not significant (NS) by two-sided Student's *t*-test.

level, IL-7Rα, Tcf1 and Eomes were more highly expressed in WT $CD8^+$ T_{CM} than WT $CD8^+$ T_{EM} cells and were more strongly induced in *Tle3*$^{-/-}$ $CD8^+$ T_{EM} cells than *Tle3*$^{-/-}$ $CD8^+$ T_{CM} cells (Fig. 3f). $CD8^+$ T_{EM} cell-associated KLRG1 and CX3CR1 showed lower expression in *Tle3*$^{-/-}$ $CD8^+$ T_{EM} and *Tle3*$^{-/-}$ $CD8^+$ T_{CM} cells compared to their WT counterparts (Fig. 3g). These analyses indicated that Tle3 exerted dual functions, that is, promoting $CD8^+$ T_{EM} but suppressing $CD8^+$ T_{CM} cell transcriptional programs.

De novo Tle3 binding promotes T_{EM} cell chromatin opening

We next profiled chromatin accessibility (ChrAcc) landscape in WT and *Tle3*$^{-/-}$ $CD8^+$ T_{CM} and $CD8^+$ T_{EM} cells using the assay for transposase-accessible chromatin with sequencing (ATAC-seq). PCA placed WT $CD8^+$ T_{CM} and WT $CD8^+$ T_{EM} cells in distinct clusters, and a direct comparison identified 1,881 T_{CM} and 2,643 T_{EM} cell signature ChrAcc sites (Fig. 4a,b). *Tle3*$^{-/-}$ $CD8^+$ T_{CM} and *Tle3*$^{-/-}$ $CD8^+$ T_{EM} cells tended to cluster

https://doi.org/10.1038/s41590-023-01720-w

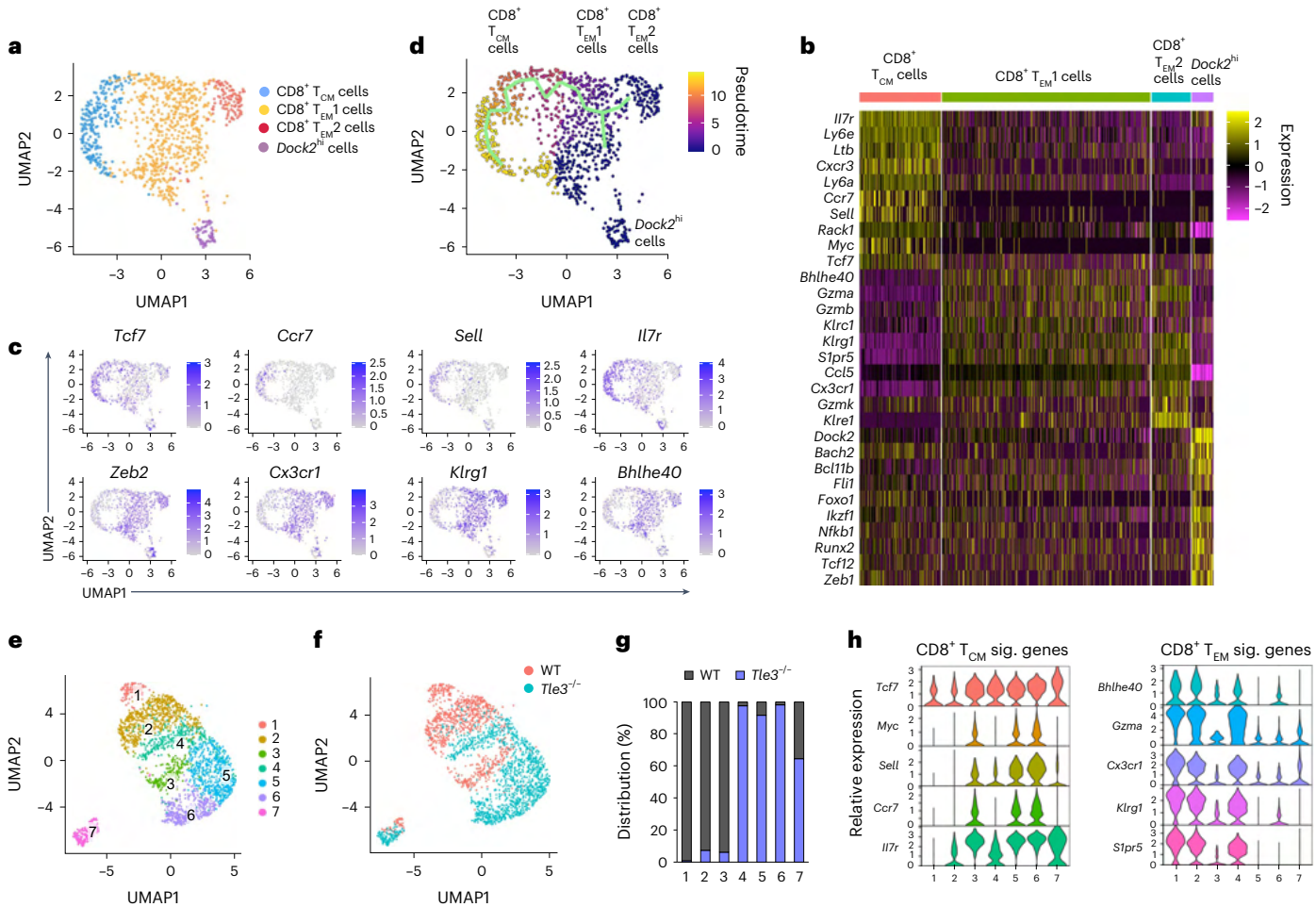

Fig. 2 | Deletion of *Tle3* promotes the formation of T_{CM} cells as manifested at the single-cell level. a, Uniform manifold approximation and projection (UMAP) plot of scRNA-seq data from WT CD45.2$^+$P14$^+$CD8$^+$ memory T cells sorted on day 30 after infection from the spleens of CD45.1 WT recipients that were adoptively transferred with WT CD45.2$^+$P14$^+$CD8$^+$ T_N cells and infected with LCMV-Arm the next day, with each dot representing a single cell and all four clusters identified with Seurat in distinct colors. **b**, Heat map showing expression of ten selected characteristic genes in CD8$^+$ T_{CM}, T_{EM}1-T_{EM}2 and *Dock2*^{hi} clusters as defined in **a**, with each column corresponding to a single cell and color scale representing *z*-score-transformed transcript levels. **c**, UMAP plot showing single-cell transcript levels of T_{CM} (top) and T_{EM} (bottom) cell signature genes, with color scale showing the range of transcript levels for each gene. **d**, Pseudotime analysis of WT CD45.2$^+$P14$^+$CD8$^+$ memory T cells using Monocle v3, with the green line denoting the trajectory. **e**,**f**, UMAP plots of scRNA-seq data from WT and *Tle3*$^{-/-}$ CD45.2$^+$P14$^+$CD8$^+$ memory T cells sorted on day 30 after infection as in **a**, displayed as clusters identified with Seurat (**e**) or single cells defined by genotype (**f**). **g**, Bar graph showing distribution of WT and *Tle3*$^{-/-}$ memory CD8$^+$ T cells in each cluster defined in **e**. **h**, Violin plots showing transcript levels of T_{CM} and T_{EM} cell signature genes in each cluster defined in **e**.

together toward WT CD8$^+$ T_{CM} cells on the PCA (Fig. 4a). A total of 5,553 differential ChrAcc sites between WT and *Tle3*$^{-/-}$ memory CD8$^+$ T cells were resolved by *k*-means into eight clusters (ChrAccC1–ChrAccC8; Fig. 4c and Extended Data Fig. 4a). ChrAcc sites in ChrAccC1–ChrAccC5 showed increased chromatin opening in *Tle3*$^{-/-}$ CD8$^+$ T_{CM} and *Tle3*$^{-/-}$ CD8$^+$ T_{EM} cells (defined as 'Tle3-closed sites'), with those in ChrAccC4 and ChrAccC5 more enriched with T_{CM} cell signature sites (Fig. 4c). In contrast, ChrAcc sites in ChrAccC6–ChrAccC8 showed decreased chromatin opening in *Tle3*$^{-/-}$ CD8$^+$ T_{CM} and *Tle3*$^{-/-}$ CD8$^+$ T_{EM} cells (defined as 'Tle3-opened sites'), with those in ChrAccC6 frequently overlapping with T_{EM} cell signature sites (Fig. 4c). Thus, Tle3 exhibited dual functions of promoting a CD8$^+$ T_{EM} but suppressing a CD8$^+$ T_{CM} cell ChrAcc landscape.

To discern the direct actions by Tle3, we used Cleavage Under Targets and Release Using Nuclease (CUT&RUN)[32] to map genome-wide Tle3 binding sites in CD62L$^+$CD44^{int-lo}CD8$^+$ T_N cells from uninfected mice, and KLRG1^{hi}IL-7Rα$^-$CD8$^+$ T_{eff} cells (day 8 after infection), CD62L$^-$CD8$^+$ T_{EM} and CD62L$^+$CD8$^+$ T_{CM} cells (day 30 after infection) from mice infected with LCMV-Arm. Each cell type formed distinct clusters on PCA (Extended Data Fig. 4b), and all four cell types had 34,292 Tle3 binding sites as determined with MACS2 (ref. 33). By applying stringent criteria (≥3-fold changes in binding strength and false discovery rate (FDR) < 0.05) in DEseq2 (ref. 34), 3,627 Tle3 binding sites exhibited significant gain or loss in binding strength in CD8$^+$ T_{eff}, T_{EM} and T_{CM} cells compared with CD8$^+$ T_N cells, and these dynamic Tle3 binding sites were distributed into three major clusters (TleC1–TleC3; Fig. 4d and Extended Data Fig. 4c). Tle3 binding sites in TleC1 were absent or weak in CD8$^+$ T_N cells, but became strong in CD8$^+$ T_{eff} cells, and were defined as 'T_{eff}-acquired sites' (Fig. 4d). Based on their binding strength in CD8$^+$ T_{EM} and CD8$^+$ T_{CM} cells, four subclusters (TleC1a–TleC1d) were distinguishable, with TleC1b and TleC1c sites retaining strong Tle3 binding in CD8$^+$ T_{EM} cells but attenuated in CD8$^+$ T_{CM} cells (Fig. 4d). These 'T_{eff}-acquired sites' were linked to genes in 'immune system processes' as determined with GREAT analysis[35] (Extended Data Fig. 4d), as observed upstream of *Tbx21* (encoding Tbet) and *Ifng* genes in the cytotoxic program (Extended Data Fig. 4e). Tle3 binding sites in TleC2 were weak in CD8$^+$ T_N cells but acquired stronger binding in CD8$^+$ T_{EM} and/or CD8$^+$ T_{CM} cells than CD8$^+$ T_{eff} cells, and were defined as 'T_M-preferred sites' (Fig. 4d), as exemplified in the *Tbx21* introns (Extended Data Fig. 4d). In contrast,

https://doi.org/10.1038/s41590-023-01720-w

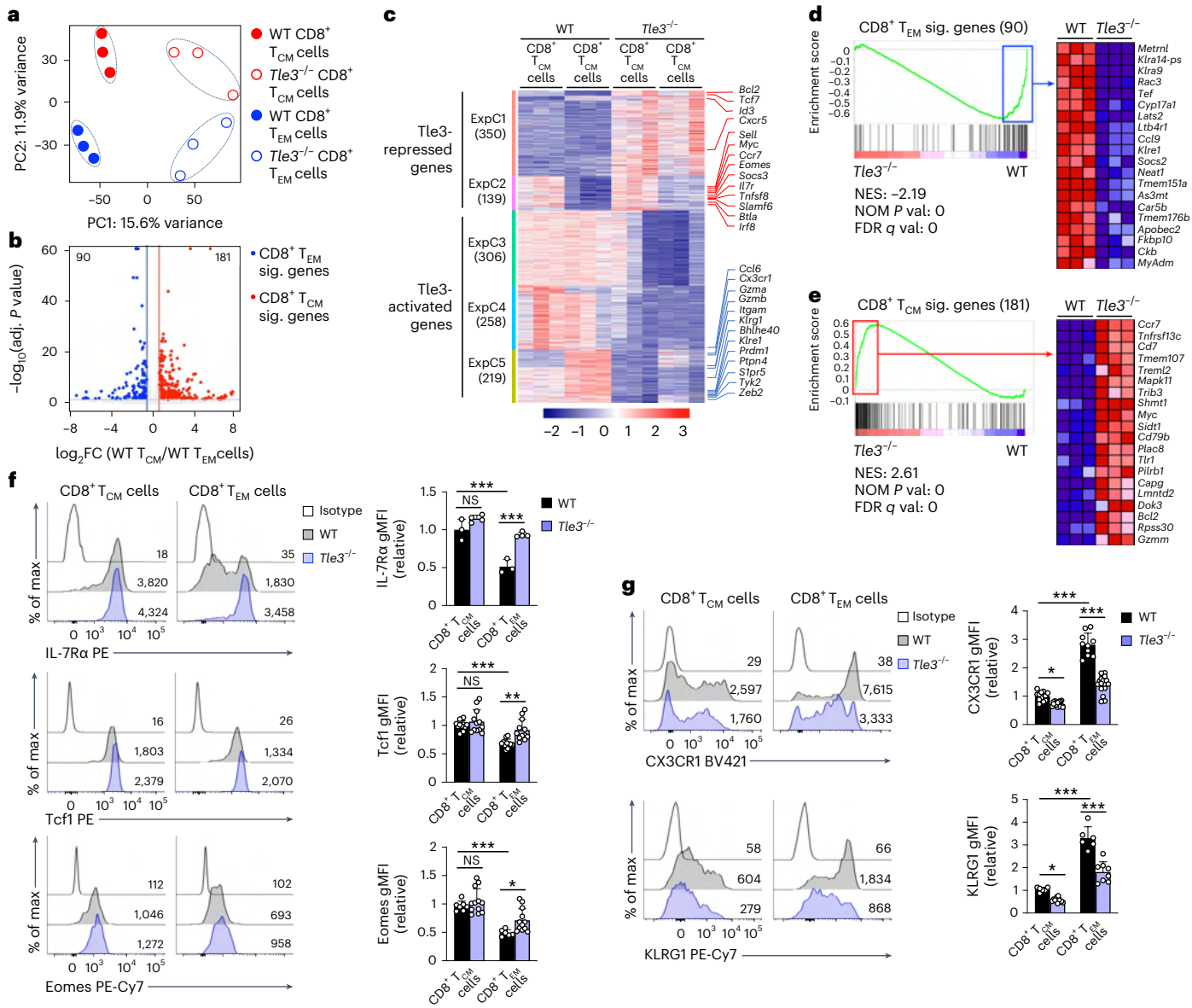

Fig. 3 | Targeting Tle3 promotes T_{CM} cell signature gene expression but diminishes $CD8^+$ T_{EM} cell signature gene expression. a, PCA of RNA-seq libraries from WT and *Tle3*$^{-/-}$ $CD45.2^+P14^+CD62L^-CD8^+$ T_{EM} cells and WT and *Tle3*$^{-/-}$ $CD45.2^+P14^+CD62L^+CD8^+$ T_{CM} cells sorted on day 30 after infection from the spleens of CD45.1 WT recipients that were adoptively transferred with WT or *Tle3*$^{-/-}$ $CD45.2^+P14^+CD8^+$ T_N cells and infected with LCMV-Arm the next day. **b**, Volcano plot showing DEGs between WT $CD8^+$ T_{CM} and WT $CD8^+$ T_{EM} cells as in **a**, by the criteria of ≥1.5-fold changes, FDR < 0.05 and fragments per kilobase of transcripts per million mapped reads (FPKM) values ≥ 0.5 in the higher-expression condition, with values denoting DEG numbers. **c**, Heat map showing five expression clusters (ExpC) identified with *k*-means clustering analysis of DEGs between WT and *Tle3*$^{-/-}$ $CD8^+$ T_{CM} cells and those between WT and *Tle3*$^{-/-}$ $CD8^+$ T_{EM} cells as in **a**, with values in parentheses denoting DEG numbers in each cluster and select T_{CM} (red line) and T_{EM} (blue line) cell signature genes marked. **d**,**e**, Enrichment plots of T_{EM} (**d**) and T_{CM} (**e**) cell signature gene sets defined in **b** in comparison of *Tle3*$^{-/-}$ versus WT $CD8^+$ T_{EM} cell transcriptomes with GSEA, with top 20 genes in the leading edge shown in heat maps. NES, normalized enrichment score; NOM *P* value and nominal *P* values were defined in GSEA. **f**,**g**, Representative half-stacked histograms showing the expression of $CD8^+$ T_{CM} cell-characteristic proteins, IL-7Rα, Tcf1 and Eomes (**f**) and that of $CD8^+$ T_{CM} cell-characteristic proteins, CX3CR1 and KLRG1 (**g**) in WT and *Tle3*$^{-/-}$ $CD8^+$ T_{CM} and T_{EM} cells identified on ≥ day 30 after infection in mice as in **a**, with values denoting gMFI for each protein, and bar graphs showing cumulative data of relative expression of each protein as means ± s.d. from 2–3 independent experiments. Statistical significance for these multiple-group comparisons was first determined with one-way ANOVA, and Tukey's test was used as post hoc correction for indicated pairwise comparison. **P* < 0.05; ***P* < 0.01; ****P* < 0.001. NS, not statistically significant.

Tle3 binding sites in TleC3 were strong in $CD8^+$ T_N cells but substantially weakened in $CD8^+$ T_{eff} cells, and were defined as 'T_{eff}-attenuated sites' (Fig. 4d). In five distinguishable subclusters (TleC3a–TleC3e) among the 'T_{eff}-attenuated sites', Tle3 binding strength in TleC3b–TleC3d sites was partly restored in $CD8^+$ T_{CM} cells (Fig. 4d). These 'T_{eff}-attenuated sites' were linked to genes in 'immune system processes' (Extended Data Fig. 4f), especially memory-characteristic genes, such as *Ccr7* and *Zeb1* (Extended Data Fig. 4g). By examining the ±100-kb regions flanking transcription start sites (TSSs) of DEGs between WT and *Tle3*$^{-/-}$ memory $CD8^+$ T cells, the dynamic Tle3 binding sites in TleC1–TleC3 were associated with ~40–60% of Tle3-repressed or Tle3-activated genes, and were mostly distributed in distal regulatory regions (Extended Data Fig. 4h,i). Thus, Tle3 was actively redeployed in the T cell genome to meet the functional needs during $CD8^+$ T cell differentiation.

When we stratified the dynamic Tle3 binding clusters (Fig. 4d) with the differential ChrAcc clusters (Fig. 4c), Tle3-opened chromatin sites in ChrAccC6 and ChrAccC7 were highly enriched in 'T_{eff}-acquired' Tle3 binding sites (TleC1a–TleC1c; Fig. 4e); in contrast, Tle3-closed chromatin sites in ChrAccC1–ChrAccC5 frequently overlapped with 'T_{eff}-attenuated' Tle3 binding sites (TleC3a–TleC3d; Fig. 4e). As exemplified at the T_{EM} cell signature genes, such as *Klrg1*, *Cx3cr1*, *Prdm1* and *Bhlhe40*, Tle3 acquired de novo binding sites in $CD8^+$ T_{eff} and $CD8^+$ T_{EM} cells, and these sites showed evidently decreased ChrAcc in *Tle3*$^{-/-}$ $CD8^+$ T_{EM} and $CD8^+$ T_{CM} cells compared to their WT counterparts (Fig. 4f). Thus, Tle3 directly contributed to establishing and/or maintaining chromatin open state, especially at genes associated with the $CD8^+$ T_{EM} cell transcriptional program.

Tle3 engages Tbet to promote T_{EM} features

We next investigated how Tle3 achieved positive control of ChrAcc. De novo motif analysis with HOMER[36] showed that the 'T_{eff}-acquired' Tle3-bound, Tle3-opened ChrAcc sites were enriched in binding motifs for the transcription factors Ets, Runx and Tbet (Fig. 5a). Runx, but not Tbet, is known to interact with Tle cofactors[37,38]. FLAG-tagged Tbet coimmunoprecipitated with HA-tagged Tle3 in 293T cells and with endogenous Tle3 in primary $CD8^+$ T_{eff} cells (Fig. 5b,c), indicating a physical interaction between Tle3 and Tbet. To further determine the cooperativity of Tle3 with Tbet and Runx3, we used CUT&RUN and identified 15,498 Runx3 binding sites and 21,354 Tbet binding sites in WT $CD8^+$ T_{eff} cells sorted on day 8 after infection with LCMV-Arm. Tle3 bound to 17,875 genomic locations in $CD8^+$ T_{eff} cells, with 65% co-occupied by Runx3 and 81% co-occupied by Tbet, and Tle3 colocalized with both Runx3 and Tbet at 54% of its binding locations (Fig. 5d), suggesting formation of multipartite complexes. Further, 63% of 'T_{eff}-acquired' Tle3 binding sites (TleC1a–TleC1d) showed colocalization with both Tbet and Runx3 (Fig. 5e), corroborating that Tle3 functioned as a cofactor of Runx3 and Tbet.

To further substantiate this point, we generated P14$^+$*hCD2-Cre*$^+$ Rosa26^{GFP} *Tbx21*$^{fl/fl}$*Runx3*$^{fl/fl}$ mice (hereafter TRKO) and P14$^+$*hCD2-Cre*$^+$*Rosa26*^{GFP}*Tbx21*$^{+/+}$*Runx3*$^{+/+}$ (hereafter WT) mice, in which *hCD2-Cre* deletes floxed alleles in mature $CD8^+$ T_N cells[39]. WT or TRKO P14$^+$$CD8^+$ T_N cells were adoptively transferred followed by LCMV-Arm infection as above, and Tle3 CUT&RUN was performed on early CD45.2$^+$P14$^+$$CD8^+$ T_{eff} cells sorted from recipient mice on day 4 after infection. WT and TRKO $CD8^+$ T_{eff} cells showed distinct Tle3 binding profiles (Extended Data Fig. 5a), with >3,000 Tle3 binding sites exhibiting diminished binding strength in TRKO compared to WT T_{eff} cells (Fig. 5f). These Tbet- and Runx3-dependent Tle3 binding sites frequently colocalized with Tbet and Runx3 in $CD8^+$ T_{eff} sites, as observed in $CD8^+$ T_{EM} cell-characteristic genes, such as *Ifng*, *Gzmb*, *Klrg1* and *Prdm1* (Fig. 5g). To specifically assess the contribution of Tbet to Tle3 binding events, we generated P14$^+$*hCD2-Cre*$^+$Rosa26^{GFP}*Tbx21*$^{fl/fl}$ mice (hereafter TbetKO), and adoptively transferred WT or TbetKO P14$^+$$CD8^+$ T_N cells followed by LCMV-Arm infection as above. Tle3 CUT&RUN was performed on early CD45.2$^+$P14$^+$$CD8^+$ T_{eff} cells sorted on day 6 after infection. While 22,467 Tle3 binding sites were called in WT $CD8^+$ T_{eff} cells, 13,393 Tle3 sites were identified in TbetKO $CD8^+$ T_{eff} cells (Extended Data Fig. 5b). Indeed, the 9,926 WT-specific Tle3 binding sites had only weak or background signals at the corresponding genomic locations in TbetKO $CD8^+$ T_{eff} cells and vice versa (Extended Data Fig. 5c), indicating a global loss of Tle3 binding in the absence of Tbet. The 3,380 Tbet- and Runx3-dependent Tle3 binding sites (defined in Fig. 5f) had attenuated binding strength in TbetKO compared to WT $CD8^+$ T_{eff} cells (Extended Data Fig. 5d), as specifically observed at T_{eff}-associated genes, including *Ifng*, *Gzma*, *Gzmb*, *Cx3cr1*, *Irf4* and *Prdm1* (Extended Data Fig. 5e). Thus, Tbet and Runx3 are both critical for Tle3 recruitment and stabilized binding.

We next investigated the direct connection of Tle3–Tbet/Runx3 complexes with $CD8^+$ T_{EM} cell molecular features. Among the 1,211 T_{EM} cell signature ChrAcc sites that overlapped with 'Tle3-opened' ChrAccC6 and ChrAccC7 sites (Fig. 4c), 204 overlapped with 'T_{eff}-acquired' Tle3 binding sites, with 54% co-occupied by Tbet and 41% by both Tbet and Runx3 (Fig. 5h). Analysis of ±100 kb regions flanking the TSS of DEGs indicated that the 'T_{eff}-acquired' Tle3-bound, Tle3-opened ChrAcc sites were predominantly associated with Tle3-activated genes (Fig. 5i). Loss of Tle3 resulted in concordant reduction in ChrAcc and gene expression in DEGs comparing WT and *Tle3*$^{-/-}$ $CD8^+$ T_{EM} cells (Fig. 5j), as observed at T_{EM} cell signature genes, such as *Klrg1*, *Cx3cr1*, *Prdm1* and *Bhlhe40* (Fig. 4f). RNA-seq analysis of WT, TbetKO, P14$^+$*hCD2-Cre*$^+$Rosa26^{GFP} *Runx3*$^{fl/fl}$ (Runx3KO) and TRKO early $CD8^+$ T_{eff} cells isolated on day 4 after infection validated that several Tle3-activated T_{EM} cell signature genes, such as *Klrg1*, *Esm1* and *S1pr5*, had decreased expression in TbetKO and TRKO compared to WT $CD8^+$ T_{eff} cells (Fig. 5k). Thus, Tle3 forms complexes with Tbet and/or Runx3 to cooperatively establish $CD8^+$ T_{EM} cell molecular features.

The 'T_{eff}-attenuated' Tle3 binding sites in TleC3 frequently overlapped with Tle3-closed chromatin sites in ChrAccC1–ChrAccC5 (Fig. 4e), and these overlapping sites were enriched in Runx, Tcf/Lef and Ets motifs (Extended Data Fig. 6a). Among the 692 $CD8^+$ T_{CM} cell signature ChrAcc sites that overlapped with 'Tle3-closed' ChrAccC1–ChrAccC5 sites (Fig. 4c), 127 sites overlapped with 'T_{eff}-attenuated' Tle3 binding sites, with 95% pre-bound by Tcf1 in $CD8^+$ T_N cells[40,41] and 28% co-occupied by Runx3 in $CD8^+$ T_{eff} cells (Extended Data Fig. 6b). Analysis of ±100 kb regions flanking the TSS of DEGs showed the 'T_{eff}-attenuated' Tle3-bound, Tle3-closed ChrAcc sites were associated with both Tle3-activated and Tle3-repressed genes (Fig. 5i). Loss of Tle3 led to a concordant increase in ChrAcc and gene expression in DEGs comparing WT and *Tle3*$^{-/-}$ $CD8^+$ T_{EM} cells (Fig. 5j), as observed in *Itgae* (encoding CD103) and T_{CM} cell signature genes, including *Ccr7*, *Tcf7*, *Sell* and *Id3* (Extended Data Fig. 6c,d). Additionally, some Tle3-closed ChrAcc sites were associated with downregulated genes, such as *Il2ra*, in *Tle3*$^{-/-}$ compared to WT $CD8^+$ T_{EM} cells (Fig. 5i,j and Extended Data Fig. 6e), suggesting induction of silencer activity upon loss of Tle3. Regardless of transcriptional outcome, these DEG-associated, 'T_{eff}-attenuated' Tle3-bound, Tle3-closed ChrAcc sites were mostly co-occupied by Tcf1 and Runx3 (Extended Data Fig. 6c–e). Thus, Tle3 co-opts Tcf1 and Runx3 to restrain $CD8^+$ T_{CM} cell molecular features, especially in $CD8^+$ T_{EM} cells.

Fig. 4 | Tle3 promotes T_{EM} cell-characteristic open chromatin profile by acquiring novel binding sites. a, PCA of ATAC-seq libraries from WT and *Tle3*$^{-/-}$ $CD8^+$ T_{CM} and $CD8^+$ T_{EM} cells sorted on day 30 after infection as in Fig. 3a. **b**, Volcano plot showing differential ChrAcc sites between WT $CD8^+$ T_{CM} and WT $CD8^+$ T_{EM} cells by the criteria of ≥2-fold changes and FDR < 0.05 as determined with DESeq2, with values denoting numbers of T_{CM} and T_{EM} cell signature ChrAcc sites. **c**, Heat map showing the eight ChrAcc clusters identified with *k*-means clustering analysis of differential ChrAcc sites between WT and *Tle3*$^{-/-}$ $CD8^+$ T_{CM} cells and those between WT and *Tle3*$^{-/-}$ $CD8^+$ T_{EM} cells as in **a**, with values in parentheses denoting site numbers in each cluster, and T_{CM} (red line) and T_{EM} (blue line) cell signature ChrAcc sites (defined in **b**) marked. **d**, Heat maps showing three major Tle3 binding clusters and associated subclusters of dynamic Tle3 binding sites identified with CUT&RUN in WT $CD8^+$ T_N cells from uninfected mice, WT $CD8^+$ T_{eff} cells sorted on day 8 after infection and WT $CD8^+$ T_{EM} and T_{CM} cells sorted on day 30 after infection from the spleens of CD45.1 WT recipients that were adoptively transferred with WT CD45.2$^+$P14$^+$$CD8^+$ T_N cells and infected with LCMV-Arm the next day, by the criteria of ≥3-fold changes, FDR < 0.05 in comparisons of $CD8^+$ T_{eff}, T_{EM} and T_{CM} with $CD8^+$ T_N cells, with values in parentheses denoting site numbers, and each row representing *z*-score-normalized Tle3 binding strength across cell types. **e**, Correlation matrix of differential ChrAcc clusters as in **c** and dynamic Tle3 binding clusters as in **d**, with values in each element denoting the numbers of overlapping sites. **f**, Sequencing tracks of Tle3 CUT&RUN and ATAC-seq at $CD8^+$ T_{EM} cell-characteristic genes as displayed on Integrative Genomics Viewer, with open bars denoting 'T_{eff}-acquired' Tle3 binding sites and Tle3-opened ChrAcc sites, and Tle3 binding subcluster information marked on the top.

https://doi.org/10.1038/s41590-023-01720-w

Targeting Tle3 reprograms memory CD8$^+$ T cell fates

Next, we performed lineage-tracing studies to investigate if Tle3 affected memory CD8$^+$ T cell plasticity and/or fate decision. CD8$^+$ T_{EM} cells convert to CD8$^+$ T_{CM} cells over time[5,10]. We sorted WT or *Tle3*$^{-/-}$ early-stage CD45.2$^+$CD62L$^-$P14$^+$CD8$^+$ T_{EM} and CD45.2$^+$CD62L$^+$P14$^+$CD8$^+$ T_{CM} cells on day 14 after infection with LCMV-Arm, and transferred them separately in equal numbers into infection-matched CD45.1 WT mice. On day 20 after transfer, donor-derived WT and *Tle3*$^{-/-}$ T_{CM} cells mostly persisted as CD62L$^+$CD8$^+$ T cells in the recipient mice (Fig. 6a). While ~1/4 of donor-derived WT CD8$^+$ T_{EM} cells became CD62L$^+$, about half of donor-derived *Tle3*$^{-/-}$ CD8$^+$ T_{EM} cells adopted the CD62L$^+$ phenotype (Fig. 6a). Similar results were obtained when the 'established' WT or

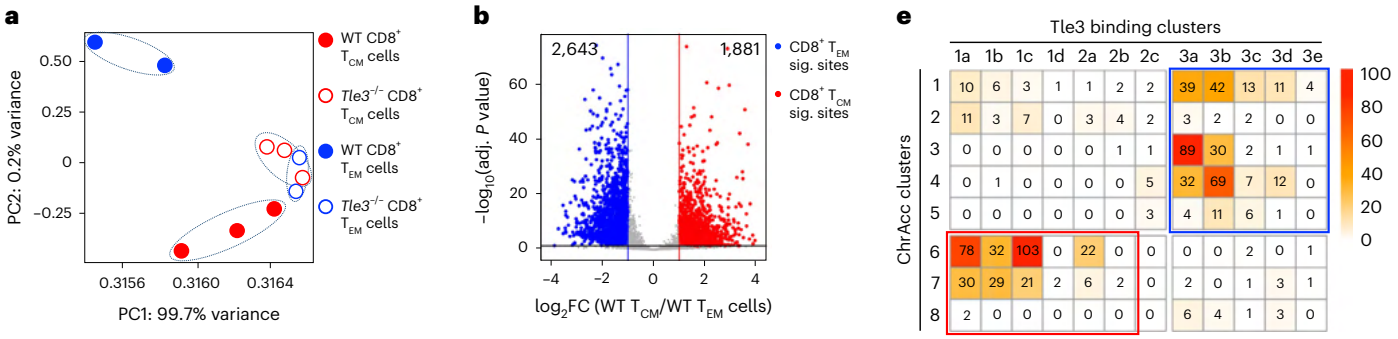

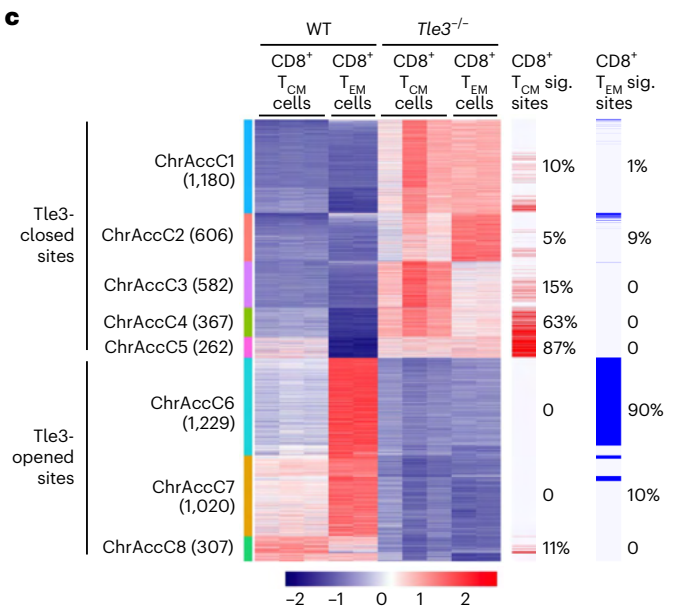

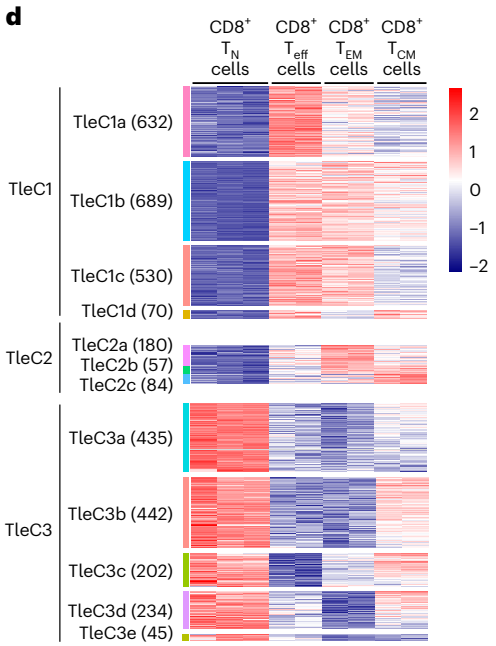

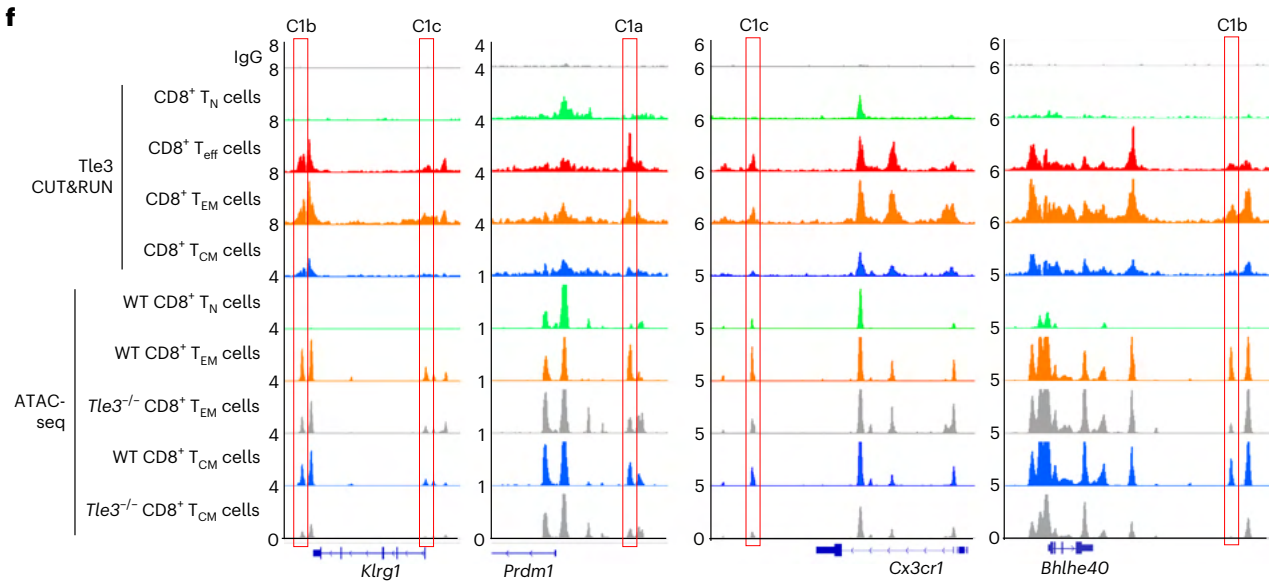

https://doi.org/10.1038/s41590-023-01720-w

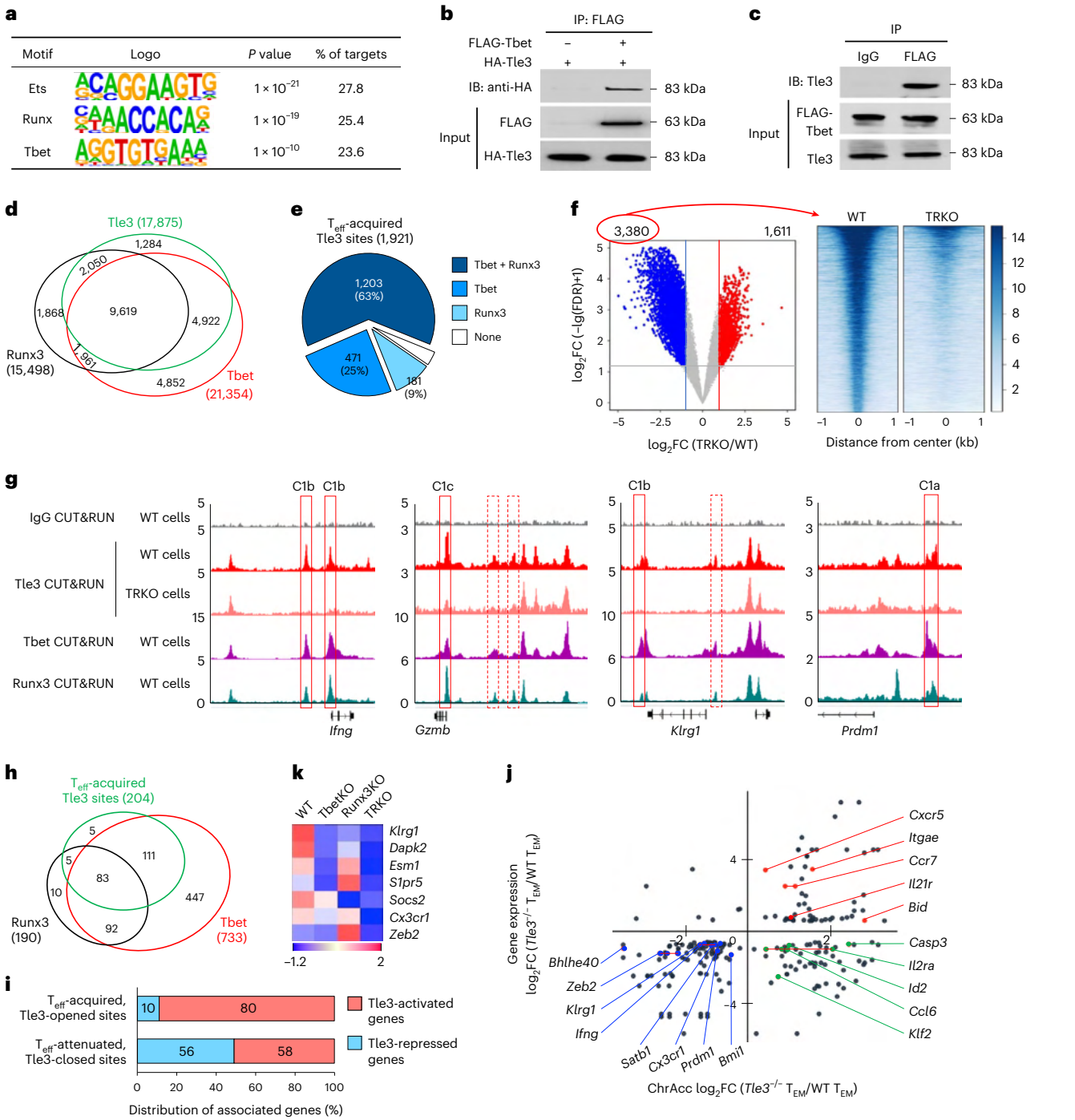

Fig. 5 | Tle3 is a coactivator of Tbet to positively regulate CD8$^+$ T_{EM} cell-characteristic molecular features. a, De novo motif analysis of ChrAccC6–ChrAccC8 sites that overlapped with 'T_{eff}-acquired' Tle3 binding sites as in Fig. 4e, with *P* values determined using HOMER. **b**,**c**, Coimmunoprecipitation of FLAG-tagged Tbet with HA-tagged Tle3 when coexpressed in 293T cells (**b**) or with endogenous Tle3 in WT CD45.2$^+$P14$^+$CD8$^+$ T_{eff} cells sorted on day 6 after infection as in Fig. 4d. IP, immunoprecipitation; IB, immunoblotting. Immunoblots are representative of two experiments **d**, Venn diagram of Tle3 binding sites with Runx3 and Tbet binding sites determined with CUT&RUN in WT CD45.2$^+$P14$^+$CD8$^+$ T_{eff} cells sorted on day 8 after infection as in Fig. 4d. **e**, Pie chart of overlapping rates of 'T_{eff}-acquired' Tle3 binding sites (TleC1a–TleC1d in Fig. 4d) with Tbet and Runx3 binding sites in CD8$^+$ T_{eff} cells as in **d**. **f**, Volcano plot showing differential Tle3 binding sites between WT and TRKO early CD45.2$^+$P14$^+$CD8$^+$ T_{eff} cells isolated on day 4 after infection from the spleens of CD45.1 WT recipients that were adoptively transferred with WT or TRKO CD45.2$^+$P14$^+$CD8$^+$ T_N cells and infected with LCMV-Arm the next day, with values denoting site numbers, and heat map showing Tle3 binding strength of the Tbet/Runx3-dependent Tle3 binding sites in WT and TRKO CD8$^+$ T_{eff} cells. **g**, Sequencing tracks of Tle3 CUT&RUN in WT and TRKO CD8$^+$ T_{eff} cells (as in **f**), Tbet and Runx3 CUT&RUN in WT CD8$^+$ T_{eff} cells (as in **d**) at CD8$^+$ T_{EM} cell-characteristic genes as displayed on Integrative Genomics Viewer, with IgG CUT&RUN tracks as a negative control. Open bars indicate Tbet/Runx3-dependent Tle3 binding sites; bars with solid lines indciate overlap with 'T_{eff}-acquired' Tle3 binding sites; Tle3 binding subcluster information is marked on the top. **h**, Venn diagram of Tle3, Tbet and Runx3 binding sites at Tle3-opened CD8$^+$ T_{EM} cell signature ChrAcc sites (defined in Fig. 4c). **i**, Bar graph showing association of dynamic Tle3-bound, Tle3-opened and Tle3-closed ChrAcc sites (defined in Fig. 4e) with Tle3-activated and Tle3-repressed genes (defined in Fig. 3c). **j**, Scatterplot showing the connection of dynamic Tle3-bound, differential ChrAcc sites with DEGs between WT and *Tle3*$^{-/-}$ CD8$^+$ T_{EM} cells, with select genes marked. **k**, Heat map showing relative expression of select Tle3-dependent CD8$^+$ T_{EM} cell signature genes in WT, TbetKO, Runx3KO and TRKO early CD45.2$^+$P14$^+$CD8$^+$ T_{eff} cells isolated on day 4 after infection as in **f**, as determined with RNA-seq analysis.

https://doi.org/10.1038/s41590-023-01720-w

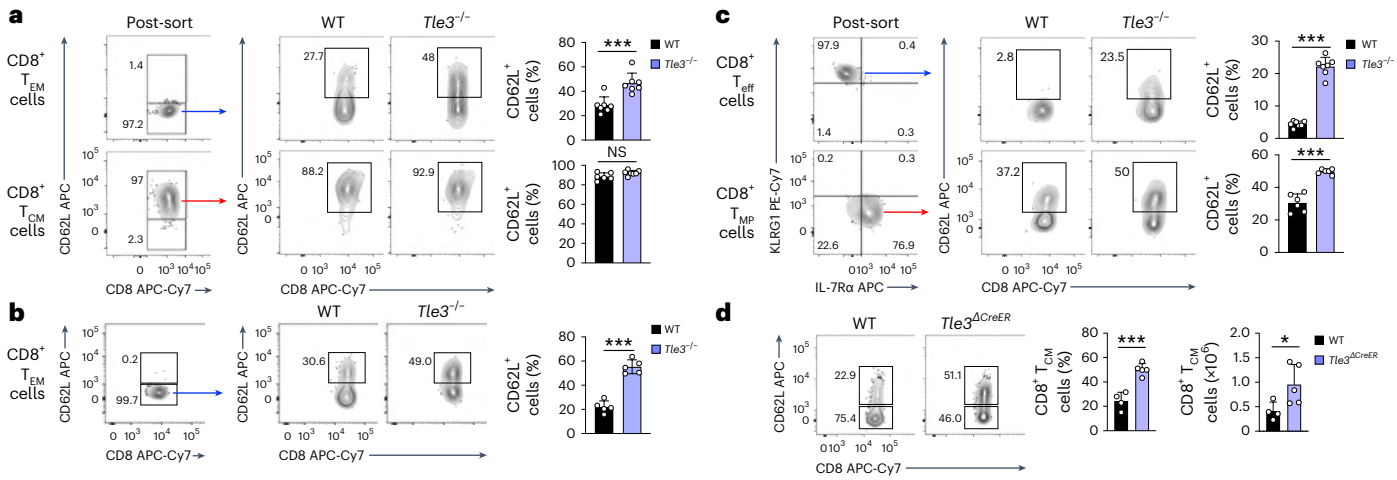

Fig. 6 | Tle3 deficiency promotes CD8$^+$ T_{CM} cell formation at all response stages. a,**b**, Representative flow cytometry plots of WT and *Tle3*$^{-/-}$ CD45.2$^+$P14$^+$CD8$^+$ memory T cells on day 20 after transfer in the spleens of infection-matched CD45.1 WT recipient mice that were adoptively transferred with WT or *Tle3*$^{-/-}$ CD45.2$^+$P14$^+$CD62L$^-$CD8$^+$ T_{EM} cells (5×10^5 cells per recipient) or CD45.2$^+$P14$^+$CD62L$^+$CD8$^+$ T_{CM} cells (3×10^5 cells per recipient) sorted on day 14 (**a**) or day 30 (**b**) after infection from the primary recipient mice generated as in Fig. 1c, and bar graphs showing cumulative data of frequency of CD62L$^+$CD8$^+$ T cells. **c**, Representative flow cytometry plots of WT and *Tle3*$^{-/-}$ CD45.2$^+$P14$^+$CD8$^+$ memory T cells on day 15 after transfer in the spleens of infection-matched CD45.1 WT recipient mice that were adoptively transferred with WT or *Tle3*$^{-/-}$ CD45.2$^+$P14$^+$KLRG1^{hi}IL-7Rα$^-$CD8$^+$ T_{eff} cells (1.5×10^6 cells per recipient) and CD45.2$^+$P14$^+$KLRG1^{lo}IL-7Rα$^+$CD8$^+$ T_{MP} cells (3×10^5 cells per recipient) sorted on day 8 after infection from primary recipient mice as in Fig. 1c, and bar graphs showing cumulative data of frequency of CD62L$^+$CD8$^+$ T cells. **d**, Representative flow cytometry plots of WT and *Tle3*$^{\Delta CreER}$ CD45.2$^+$P14$^+$CD8$^+$ memory T cells on day 35 after infection in the spleens of CD45.1 WT mice that were adoptively transferred with CD45.2$^+$P14$^+$CreER$^+$*Tle3*$^{+/+}$ or CD45.2$^+$P14$^+$CreER$^+$*Tle3*$^{fl/fl}$ CD8$^+$ T_N cells, infected with LCMV-Arm the next day, and treated with tamoxifen on days 6, 7 and 21 after infection, and bar graphs showing cumulative data of frequency and numbers of WT or *Tle3*$^{\Delta CreER}$ CD62L$^+$CD8$^+$ T cells. All contour plots are representative of data from 2–3 experiments, and cumulative data are means ± s.d. $^{**}P < 0.01$; $^{***}P < 0.001$ by two-tailed Student's *t*-test.

Tle3$^{-/-}$ CD8$^+$ T_{EM} cells sorted on day 30 after infection were used as donor cells (Fig. 6b), indicating that conversion of CD8$^+$ T_{EM} to T_{CM} cells was accelerated upon loss of *Tle3*. We also used KLRG1^{hi}IL-7Rα$^-$P14$^+$CD8$^+$ T_{eff} cells and KLRG1^{lo}IL-7Rα$^+$P14$^+$CD8$^+$ T_{MP} cells sorted on day 8 after infection as donor cells. On day 15 after transfer, <5% WT CD8$^+$ T_{eff}-derived cells were CD62L$^+$, while ~30% of WT CD8$^+$ T_{MP}-derived cells were CD62L$^+$ (Fig. 6c). *Tle3*$^{-/-}$ CD8$^+$ T_{eff} and *Tle3*$^{-/-}$ CD8$^+$ T_{MP} cells both yielded CD62L^{hi} cells at ~25% and 50%, respectively (Fig. 6c), suggesting that targeting Tle3 increased the T_{CM}-producing capacity in both CD8$^+$ T_{eff} and CD8$^+$ T_{MP} cells.

To determine if Tle3 had continuous roles in regulating memory CD8$^+$ T cell plasticity, we generated P14$^+$CreER$^+$*Tle3*$^{fl/fl}$ and P14$^+$CreER$^+$*Tle3*$^{+/+}$ mice, and adoptively transferred CD45.2$^+$P14$^+$CD8$^+$ T_N cells into CD45.1 WT mice followed by LCMV-Arm infection as above. The recipients were treated with tamoxifen on days 6 and 7 after infection to induce CreER activity and *Tle3* ablation, and on day 21 after infection to ensure sustained *Tle3* ablation (Extended Data Fig. 7a). Two weeks after the last tamoxifen treatment, P14$^+$CreER$^+$*Tle3*$^{fl/fl}$-derived (hereafter *Tle3*$^{\Delta CreER}$) memory CD8$^+$ T cells had >2-fold increase in frequency and numbers of CD62L$^+$CD8$^+$ T_{CM} cells over P14$^+$CreER$^+$*Tle3*$^{+/+}$-derived (WT) memory CD8$^+$ cells (Fig. 6d). *Tle3*$^{\Delta CreER}$ CD8$^+$ T_{EM} cells had increased expression of T_{CM} cell-characteristic Tcf1 and Eomes proteins, but decreased expression of T_{EM} cell-characteristic CX3CR1 and KLRG1 proteins compared to

Fig. 7 | Induced *Tle3* deletion in 'established' CD8$^+$ T_{EM} cells promotes CD8$^+$ T_{CM} cell formation while sustaining its functionality. a, Volcano plot showing DEGs (≥1.5-fold expression changes, FDR < 0.05) between WT and *Tle3*$^{\Delta CreER}$ CD45.2$^+$P14$^+$CD62L$^-$CD8$^+$ T_{EM} cells treated with 4-OHT ex vivo for 48 h after purification by cell sorting on ≥ 30 day after infection from the spleens of CD45.1 WT mice that were adoptively transferred with CD45.2$^+$P14$^+$CreER$^+$*Tle3*$^{+/+}$ or CD45.2$^+$P14$^+$CreER$^+$*Tle3*$^{fl/fl}$ CD8$^+$ T_N cells and infected with LCMV-Arm the next day, with values denoting DEG numbers. **b**,**c**, Enrichment plots of T_{EM} (**b**) and T_{CM} (**c**) cell signature gene sets (defined in Fig. 3b) in the comparison of *Tle3*$^{\Delta CreER}$ versus WT CD8$^+$ T_{EM} cell transcriptomes with GSEA, with the top 20 genes in the leading edge shown in heat maps, and those in red denoting overlap with the corresponding top 20 enriched genes in Fig. 3d,e. NOM *P* values and FDR q values are defined in GSEA. **d**, Volcano plot showing differential ChrAcc sites (≥1.5-fold changes, FDR < 0.05) between WT and *Tle3*$^{\Delta CreER}$ CD45.2$^+$P14$^+$CD62L$^-$CD8$^+$ T_{EM} cells after ex vivo treatment with 4-OHT for 48 h as in **a**, with values denoting site numbers. **e**, Bar graph showing distribution of T_{CM} and T_{EM} cell signature ChrAcc sites (defined in Fig. 4b) among the overlapping differential ChrAcc sites in *Tle3*$^{\Delta CreER}$ versus WT CD8$^+$ T_{EM} cell comparison as in **d**, with values denoting site numbers. **f**, ATAC-seq tracks of WT and *Tle3*$^{\Delta CreER}$ CD8$^+$ T_{EM} cells (as in **d**) at the T_{EM} (top) and T_{CM} (bottom) cell-characteristic genes. Blue open bars indicate more 'closed' sites; red open bars indicate more 'open' sites in *Tle3*$^{\Delta CreER}$ compared to WT CD8$^+$ T_{EM} cells. **g**, Representative flow cytometry plots of WT and *Tle3*$^{\Delta CreER}$ CD45.2$^+$P14$^+$CD8$^+$ memory T cells on day 14 after transfer in the spleens of infection-matched CD45.1 WT recipient mice that were adoptively transferred with WT and *Tle3*$^{\Delta CreER}$ CD45.2$^+$P14$^+$CD8$^+$ T_{EM} cells (5×10^5 cells per recipient) sorted on day 32 after infection from the spleens of primary recipient mice that were adoptively transferred with CD45.2$^+$P14$^+$CreER$^+$*Tle3*$^{+/+}$ or CD45.2$^+$P14$^+$CreER$^+$*Tle3*$^{fl/fl}$ CD8$^+$ T_N cells, infected with LCMV-Arm the next day, and treated with tamoxifen on days 30 and 31 after infection. Bar graphs show cumulative data of frequency and numbers of WT or *Tle3*$^{\Delta CreER}$ CD62L^{hi}CD8$^+$ T cells, as means ± s.d. from two independent experiments. **h**–**j**, Bar graphs showing cell numbers (**h**), percentages of IFN-γ-producing cells (**i**) and granzyme B expression (**j**) of secondary CD8$^+$ T_{eff} cells detected on day 3 after infection in the spleens of *Rag1*$^{-/-}$ mice that were adoptive transferred with WT and *Tle3*$^{\Delta CreER}$ CD45.2$^+$P14$^+$CD62L$^+$CD8$^+$ T_{CM} cells (2×10^4 cells per recipient) sorted on day 45 after infection from the spleens of primary recipient mice as in **g** and infected with LM-GP33 the next day. **k**, Bar graph showing colony-forming units (CFUs) in the livers of *Rag1*$^{-/-}$ mice as in **h**–**j**, as means ± s.d. from one of two independent experiments. In **i**–**k**, *P* values were determined with two-tailed Student's *t*-test. $^{**}P < 0.01$.

https://doi.org/10.1038/s41590-023-01720-w

WT CD8$^+$ T_{EM} cells, while WT and *Tle3*$^{\Delta CreER}$ CD8$^+$ T_{EM} cells had similar production of IFN-γ and TNF (Extended Data Fig. 7b–d). These data suggested that persistent Tle3 expression was necessary for restraining CD8$^+$ T_{CM} cell formation.

To investigate the impact of acute *Tle3* deletion on 'established' memory CD8$^+$ T cells, CD45.2$^+$P14$^+$CD8$^+$ T_N cells from P14$^+$CreER$^+$*Tle3*$^{+/+}$ or P14$^+$CreER$^+$*Tle3*$^{fl/fl}$ mice were adoptively transferred, followed by LCMV-Arm infection as above. On day 30 after

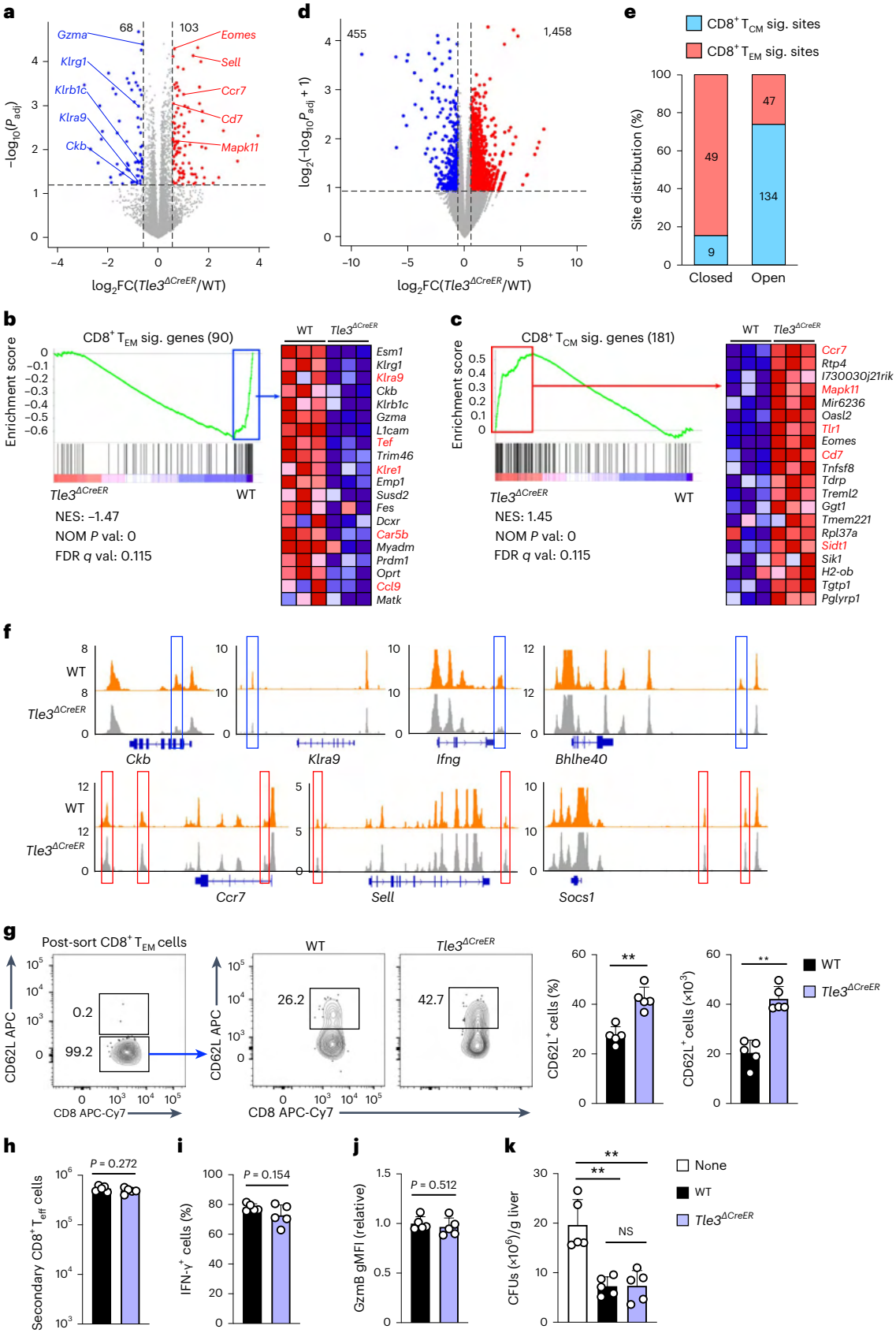

infection, sorted CD45.2$^+$CD62L$^-$CD8$^+$ T_{EM} cells were cultured ex vivo with 4-hydroxy-tamoxifen (4-OHT) for 48 h to induce *Tle3* ablation (Extended Data Fig. 8a). The resulting *Tle3*$^{\Delta CreER}$ CD8$^+$ T_{EM} cells showed effective deletion of the floxed *Tle3* exons 3–4 by RNA-seq (Extended Data Fig. 8b), and comparison with 4-OHT-treated WT CD8$^+$ T_{EM} cells identified 171 DEGs, with *Tle3*$^{\Delta CreER}$ T_{EM} cells showing reduced expression of T_{EM} cell signature genes such as *Klrg1*, *Gzma*, *Klra9* and *Ckb*, but increased expression of T_{CM} cell signature genes, including *Sell*, *Ccr7*, *Eomes* and *Mapk11* (Fig. 7a). GSEA indicated that the T_{EM} cell signature gene set was depleted, while the T_{CM} cell signature gene set was enriched in *Tle3*$^{\Delta CreER}$ compared to WT CD8$^+$ T_{EM} cells (Fig. 7b,c). We also performed ATAC-seq on WT and *Tle3*$^{\Delta CreER}$ CD8$^+$ T_{EM} cells and found that 1,458 ChrAcc sites were more 'open', while 455 sites were more 'closed' in *Tle3*$^{\Delta CreER}$ compared to WT CD8$^+$ T_{EM} cells (Fig. 7d). Approximately 12% of these differential ChrAcc sites overlapped with the T_{CM} and T_{EM} cell signature sites (Fig. 4b), and among these, the more 'closed' ChrAcc sites in *Tle3*$^{\Delta CreER}$ CD8$^+$ T_{EM} cells were enriched with T_{EM} cell signature sites, and the more 'open' ChrAcc sites in *Tle3*$^{\Delta CreER}$ CD8$^+$ T_{EM} cells were enriched with T_{CM} cell signature sites (Fig. 7e). Specifically, the more 'closed' ChrAcc sites in *Tle3*$^{\Delta CreER}$ CD8$^+$ T_{EM} cells were found at T_{EM} cell signature genes such as *Ckb* and *Klra9*, and effector function-associated genes including *Ifng* and *Bhlhe40* (Fig. 7f), while the more 'open' ChrAcc sites in *Tle3*$^{\Delta CreER}$ CD8$^+$ T_{EM} cells were observed at T_{CM} cell signature genes including *Ccr7*, *Sell* and *Socs1* (Fig. 7f). Thus, acute deletion of *Tle3* had immediate effect of diminishing CD8$^+$ T_{EM} and promoting CD8$^+$ T_{CM} cell molecular features in CD8$^+$ T_{EM} cells.

To assess the impact of acute *Tle3* deletion in vivo, mice adoptively transferred with P14$^+$CreER$^+$*Tle3*$^{+/+}$ or P14$^+$CreER$^+$*Tle3*$^{fl/fl}$ T_N cells were infected with LCMV-Arm as above and treated with tamoxifen on days 31 and 32 after infection. One day later, CD45.2$^+$CD62L$^-$CD8$^+$ T_{EM} cells were sorted and transferred into infection-matched CD45.1 WT mice (Extended Data Fig. 8a). Two weeks after transfer, CD62L$^+$ cells derived from *Tle3*$^{\Delta CreER}$ CD8$^+$ T_{EM} cells were ~1.5- to 2-fold higher in frequency and numbers than those from WT CD8$^+$ T_{EM} cells (Fig. 7g). To determine the functionality of Tle3-deficient CD8$^+$ T_{CM} cells, another cohort of tamoxifen-treated recipient mice as above were rested for 2 weeks to allow in situ CD8$^+$ T_{EM}-to-CD8$^+$ T_{CM} conversion, and WT or *Tle3*$^{\Delta CreER}$-derived CD45.2$^+$CD62L$^+$CD8$^+$ T_{CM} cells were sorted and transferred into *Rag1*$^{-/-}$ mice followed by infection with *Listeria monocytogenes* expressing the GP33 epitope (LM-GP33) (Extended Data Fig. 8a). On day 3 after *L. monocytogenes* infection, we detected similar numbers of secondary CD8$^+$ T_{eff} cells derived from WT and *Tle3*$^{\Delta CreER}$ CD8$^+$ T_{CM} cells (Fig. 7h), which had similar IFN-γ production and granzyme B expression (Fig. 7i,j). While *Listeria* expanded rapidly in *Rag1*$^{-/-}$ mice due to lack of endogenous adaptive immune responses, transfer of WT or *Tle3*$^{\Delta CreER}$ CD8$^+$ T_{CM} cells curbed bacterial expansion with similar efficacy (Fig. 7k). Additionally, *Tle3*$^{\Delta CreER}$ P14$^+$CD8$^+$ T_{CM} and T_{EM} cells showed similar capacity of curtailing the growth of subcutaneously inoculated B16 melanoma cells expressing the GP33 epitope (B16-GP33), compared to their WT counterparts[42,43] (Extended Data Fig. 8c–h). These data suggest that targeting Tle3 facilitates the production of CD8$^+$ T_{CM} cells without compromising their recall responses to pathogens or tumor antigens.

Discussion

Using integrative functional and multiomics approaches, we showed that Tle3 reciprocally regulated CD8$^+$ T_{EM} and T_{CM} cell fate decision and lineage plasticity. Tle3 acted as a gatekeeper that preserved the CD8$^+$ T_{EM} cell pool, and its persistent expression was required at all stages of CD8$^+$ T cell responses. Targeting *Tle3* accelerated the conversion of CD8$^+$ T_{EM} cells to CD8$^+$ T_{CM} cells and induced a T_{CM}-forming capacity in terminally differentiated CD8$^+$ T_{eff} cells, while the converted T_{CM} cells sustained their superior recall capacity.

The functional redundancy among the multiple Tle cofactors poses a challenge to dissecting their regulatory roles in T cell biology. Combined deletion of *Tle* genes abrogated the accumulation of antigen-specific CD8$^+$ T_{eff} cells. The effect was more severe than targeting Runx3 or Tbet alone[7,17,44], highlighting an integrative function of multiple transcription factors by Tle proteins. Here, selective targeting of *Tle3* revealed its unique requirements for sustaining the CD8$^+$ T_{EM} cell pool while restraining CD8$^+$ T_{CM} cell formation. This biological impact was likely a collective effect of perturbing multiple transcription factor complexes that were sensitive to loss of Tle3, which was not compensated by Tle1 and Tle4. Thus, transcription cofactors such as Tle had unique functions as integrators of transcription factor complexes acting downstream of various external inputs.

Longitudinal tracking of Tle3 binding during effector and memory CD8$^+$ T cell differentiation revealed dynamic redistribution of Tle3 in the CD8$^+$ T cell genome. The active gain of Tle3 binding in antigen-experienced CD8$^+$ T_{eff}, T_{EM} and T_{CM} cells was concordant with induced Tbet expression in these cells. Tle3 and Tbet physically interacted, colocalized extensively in CD8$^+$ T_{eff} cell genome, and the Tle3–Tbet cooperativity frequently involved Runx3, forming multipartite complexes. Intact expression of Tbet and Runx3 was critical for effective Tle3 recruitment and its stable engagement in the regulatory complexes. Meanwhile, Tle3 binding was attenuated in another set of genomic locations in CD8$^+$ T_{eff} and T_{EM} cells, some of which partly restored its binding in CD8$^+$ T_{CM} cells. This Tle3 binding dynamics coincided with the expression pattern of Tcf1 and Lef1, and these sites were intrinsically accessible to Tcf1, as evidenced by enrichment of Tcf/Lef binding motifs and colocalization of Tcf1 peaks identified with chromatin immunoprecipitation followed by sequencing in CD8$^+$ T_N cells. Additionally, 'T_{eff}-acquired' and 'T_{eff}-attenuated' Tle3 binding sites were both enriched in the less restrictive GGAA Ets motif, and at least ten Ets family transcription factors are abundantly expressed in T cells[45,46]. Although the identities of Tle3–Ets complexes remained unknown, our findings highlighted the advantages of characterizing Tle cofactors for their integrative regulatory roles in T cells.

Tle proteins are historically known as transcriptional repressors[22,24], and are also reported to activate transcription in adipocytes[47,48]. Our analysis indicated that Tle3 controlled an 'open' chromatin state at its direct binding sites and positive regulation of their associated genes. The Tle3–Tbet complex had a dominant role in activating CD8$^+$ T_{EM} cell-characteristic gene expression and ChrAcc landscape. In parallel, Tle3-dependent 'closed' chromatin state and gene repression contributed to restraining the activation of the CD8$^+$ T_{CM} program, where Tle3–Runx3 and Tle3–Tcf1 complexes could act through direct and indirect mechanisms. Ablating *Runx3* in CD8$^+$ T_{eff} cells caused aberrantly induced genes associated with follicular helper T cells, generating Tcf1$^+$CXCR5$^+$CD8$^+$ cells with B cell help function[17]. Compound deletion of Tcf1 together with Runx3 prevented the follicular helper T cell lineage divergence[17]. These findings reconciled with our observations and suggested that Tle–Runx3 complexes, in which all Tle proteins were likely involved, were responsible for complete repression of Tcf1 in CD8$^+$ T_{eff} cells. Specific disruption of the Tle3–Runx3 complex resulted in more nuanced regulation of Tcf1, allowing modest activation of the CD8$^+$ T_{CM} program, while avoiding the detrimental effect of ablating Runx3 or all Tle proteins[17,44]. In sum, Tle3 uses dual functions in gene regulation to guard CD8$^+$ T_{EM} cell lineage fidelity, and releasing the brake mediated by Tle3 facilitates the formation of CD8$^+$ T_{CM} cells with better durability and more robust recall capacity.

Online content

Any methods, additional references, Nature Portfolio reporting summaries, source data, extended data, supplementary information, acknowledgements, peer review information; details of author contributions and competing interests; and statements of data and code availability are available at https://doi.org/10.1038/s41590-023-01720-w.

References

1. Akondy, R. S. et al. Origin and differentiation of human memory CD8 T cells after vaccination. *Nature* **552**, 362–367 (2017).
2. Jameson, S. C. & Masopust, D. Understanding subset diversity in T cell memory. *Immunity* **48**, 214–226 (2018).
3. Martin, M. D. & Badovinac, V. P. Defining memory CD8 T cell. *Front Immunol.* **9**, 2692 (2018).
4. Sallusto, F., Lenig, D., Forster, R., Lipp, M. & Lanzavecchia, A. Two subsets of memory T lymphocytes with distinct homing potentials and effector functions. *Nature* **401**, 708–712 (1999).
5. Wherry, E. J. et al. Lineage relationship and protective immunity of memory CD8 T cell subsets. *Nat. Immunol.* **4**, 225–234 (2003).
6. Kaech, S. M. et al. Selective expression of the interleukin 7 receptor identifies effector CD8 T cells that give rise to long-lived memory cells. *Nat. Immunol.* **4**, 1191–1198 (2003).
7. Joshi, N. S. et al. Inflammation directs memory precursor and short-lived effector CD8$^+$ T cell fates via the graded expression of T-bet transcription factor. *Immunity* **27**, 281–295 (2007).
8. Lin, W. W. et al. CD8$^+$ T lymphocyte self-renewal during effector cell determination. *Cell Rep.* **17**, 1773–1782 (2016).
9. Pais Ferreira, D. et al. Central memory CD8$^+$ T cells derive from stem-like Tcf7^{hi} effector cells in the absence of cytotoxic differentiation. *Immunity* **53**, 985–1000 (2020).
10. Herndler-Brandstetter D. et al. KLRG1$^+$ effector CD8$^+$ T cells lose KLRG1, differentiate into all memory T cell lineages, and convey enhanced protective immunity. *Immunity* https://doi.org/10.1016/j.immuni.2018.03.015 (2018).
11. Chung, H. K., McDonald, B. & Kaech, S. M. The architectural design of CD8$^+$ T cell responses in acute and chronic infection: parallel structures with divergent fates. *J. Exp. Med.* **218**, e20201730 (2021).
12. Chen, Y., Zander, R., Khatun, A., Schauder, D. M. & Cui, W. Transcriptional and epigenetic regulation of effector and memory CD8 T cell differentiation. *Front Immunol.* **9**, 2826 (2018).
13. Kallies, A., Xin, A., Belz, G. T. & Nutt, S. L. Blimp-1 transcription factor is required for the differentiation of effector CD8$^+$ T cells and memory responses. *Immunity* **31**, 283–295 (2009).
14. Gautam, S. et al. The transcription factor c-Myb regulates CD8$^+$ T cell stemness and antitumor immunity. *Nat. Immunol.* **20**, 337–349 (2019).
15. Zhou, X. et al. Differentiation and persistence of memory CD8$^+$ T cells depend on T cell factor 1. *Immunity* **33**, 229–240 (2010).
16. Pipkin, M. E. Runx proteins and transcriptional mechanisms that govern memory CD8 T cell development. *Immunol. Rev.* **300**, 100–124 (2021).
17. Shan, Q. et al. The transcription factor Runx3 guards cytotoxic CD8$^+$ effector T cells against deviation towards follicular helper T cell lineage. *Nat. Immunol.* **18**, 931–939 (2017).
18. Orian, A. et al. A Myc-Groucho complex integrates EGF and Notch signaling to regulate neural development. *Proc. Natl Acad. Sci. USA* **104**, 15771–15776 (2007).
19. Ren, B., Chee, K. J., Kim, T. H. & Maniatis, T. PRDI-BF1/Blimp-1 repression is mediated by corepressors of the Groucho family of proteins. *Genes Dev.* **13**, 125–137 (1999).
20. Zhao, X., Shan, Q. & Xue, H. H. TCF1 in T cell immunity: a broadened frontier. *Nat. Rev. Immunol.* **22**, 147–157 (2022).
21. Seo, W. & Taniuchi, I. The roles of RUNX family proteins in development of immune cells. *Mol. Cells* **43**, 107–113 (2020).
22. Turki-Judeh, W. & Courey, A. J. Groucho: a corepressor with instructive roles in development. *Curr. Top. Dev. Biol.* **98**, 65–96 (2012).
23. Buscarlet, M. & Stifani, S. The 'Marx' of Groucho on development and disease. *Trends Cell Biol.* **17**, 353–361 (2007).
24. Jennings, B. H. & Ish-Horowicz, D. The Groucho/TLE/Grg family of transcriptional co-repressors. *Genome Biol.* **9**, 205 (2008).
25. Gasperowicz, M. & Otto, F. Mammalian Groucho homologs: redundancy or specificity? *J. Cell. Biochem.* **95**, 670–687 (2005).
26. Xing, S. et al. Tle corepressors are differentially partitioned to instruct CD8$^+$ T cell lineage choice and identity. *J. Exp. Med.* **215**, 2211–2226 (2018).
27. Wheat, J. C. et al. The corepressor Tle4 is a novel regulator of murine hematopoiesis and bone development. *PLoS ONE* **9**, e105557 (2014).
28. Ramasamy, S. et al. Tle1 tumor suppressor negatively regulates inflammation in vivo and modulates NF-κB inflammatory pathway. *Proc. Natl Acad. Sci. USA* **113**, 1871–1876 (2016).
29. Rutishauser, R. L. et al. Transcriptional repressor Blimp-1 promotes CD8$^+$ T cell terminal differentiation and represses the acquisition of central memory T cell properties. *Immunity* **31**, 296–308 (2009).
30. Mahajan, V. S. et al. DOCK2 sets the threshold for entry into the virtual memory CD8$^+$ T cell compartment by negatively regulating tonic TCR triggering. *J. Immunol.* **204**, 49–57 (2020).
31. Cao, J. et al. The single-cell transcriptional landscape of mammalian organogenesis. *Nature* **566**, 496–502 (2019).
32. Skene, P. J. & Henikoff, S. An efficient targeted nuclease strategy for high-resolution mapping of DNA binding sites. *Elife* **6**, e21856 (2017).
33. Zhang, Y. et al. Model-based analysis of ChIP–seq (MACS). *Genome Biol.* **9**, R137 (2008).
34. Love, M. I., Huber, W. & Anders, S. Moderated estimation of fold change and dispersion for RNA-seq data with DESeq2. *Genome Biol.* **15**, 550 (2014).
35. McLean, C. Y. et al. GREAT improves functional interpretation of cis-regulatory regions. *Nat. Biotechnol.* **28**, 495–501 (2010).
36. Heinz, S. et al. Simple combinations of lineage-determining transcription factors prime *cis*-regulatory elements required for macrophage and B cell identities. *Mol. Cell* **38**, 576–589 (2010).
37. Levanon, D. et al. Transcriptional repression by AML1 and LEF-1 is mediated by the TLE/Groucho corepressors. *Proc. Natl Acad. Sci. USA* **95**, 11590–11595 (1998).
38. Chen, G. & Courey, A. J. Groucho/TLE family proteins and transcriptional repression. *Gene* **249**, 1–16 (2000).
39. Liu, J. et al. CTCF mediates CD8$^+$ effector differentiation through dynamic redistribution and genomic reorganization. *J. Exp. Med.* **220**, e20221288 (2023).
40. Shan, Q. et al. Tcf1 and Lef1 provide constant supervision to mature CD8$^+$ T cell identity and function by organizing genomic architecture. *Nat. Commun.* **12**, 5863 (2021).
41. Shan, Q. et al. Tcf1-CTCF cooperativity shapes genomic architecture to promote CD8$^+$ T cell homeostasis. *Nat. Immunol.* **23**, 1222–1235 (2022).
42. Milner, J. J. et al. Runx3 programs CD8$^+$ T cell residency in non-lymphoid tissues and tumours. *Nature* **552**, 253–257 (2017).
43. Shan, Q. et al. Ectopic Tcf1 expression instills a stem-like program in exhausted CD8$^+$ T cells to enhance viral and tumor immunity. *Cell Mol. Immunol.* **18**, 1262–1277 (2021).
44. Wang, D. et al. The transcription factor Runx3 establishes chromatin accessibility of *cis*-regulatory landscapes that drive memory cytotoxic T lymphocyte formation. *Immunity* **48**, 659–674 (2018).
45. Sharrocks, A. D. The ETS-domain transcription factor family. *Nat. Rev. Mol. Cell Biol.* **2**, 827–837 (2001).
46. Anderson, M. K., Hernandez-Hoyos, G., Diamond, R. A. & Rothenberg, E. V. Precise developmental regulation of Ets family transcription factors during specification and commitment to the T cell lineage. *Development* **126**, 3131–3148 (1999).

47. Villanueva, C. J. et al. TLE3 is a dual-function transcriptional coregulator of adipogenesis. *Cell Metab.* **13**, 413–427 (2011).
48. Pearson, S. et al. Loss of TLE3 promotes the mitochondrial program in beige adipocytes and improves glucose metabolism. *Genes Dev.* **33**, 747–762 (2019).